Supplementary Information

Gate tunable hole charge qubit formed in a Ge/Si nanowire double quantum dot coupled to microwave photons

Rui Wang[1,2], Russell S. Deacon[1,3*], Jian Sun[1,4], Jun Yao[5], Charles M. Lieber[6,7] and Koji Ishibashi[1,3]

[1]Advanced Device Laboratory, RIKEN, Wako, Saitama 351-0198, Japan.
[2]Department of Physics, Tokyo University of Science, Kagurazaka, Tokyo 162-8601, Japan.
[3]Center for Emergent Matter Science (CEMS), RIKEN, Wako, Saitama 351-0198, Japan.
[4]Hunan Key Laboratory of Super Micro-structure and Ultrafast Process, School of Physics and Electronics, Central South University, Changsha 410083, China.
[5]Department of Electrical and Computer Engineering; Institute for Applied Life Sciences, University of Massachusetts, Amherst, Massachusetts 01003, USA
[6]Deparment of Chemistry and Chemical Biology, Harvard University, Cambridge, Massachusetts 02138, USA.
[7]School of Engineering and Applied Sciences, Harvard University, Cambridge, Massachusetts 02138, USA.
*Corresponding author. Email: russell@riken.jp

This file includes:
Supplementary Text
Figs. S1 to S6
References

Contents:
1. Device Preparation
   - Ge/Si nanowire transfer
   - hBN flakes transfer
   - Lithography
2. Measurement Setup
3. DQD Out of Equilibrium
4. Resonator Phase Spectrum with Different Qubit Decoherence
5. Resonator Signal Response with Different Coupling Strength
6. Evolution of Resonance Full Spectrum with Different Decoherence
7. Power Dependence of the Dispersive Shift

Device Preparation

Ge/Si nanowire transfer. Epitaxial Ge/Si core/shell NWs were synthesized by a two-step vapor-liquid-solid method.[1] Ge/Si NWs are typically a few microns long with 10~20nm thick core and 2~4nm thin shell. One NW is shown in a highly magnified transmission electron micrograph (TEM) in Figure S1(c), where the Ge core and Si shell interface can be easily identified from the electron transmission contrast. The individual NWs are precisely placed onto target devices by a dry transfer method using a home-made micro-manipulator, a similar technique has been reported elsewhere.[2–4] Briefly, the NWs are first dispersed in ethanol from the growth substrates by weak sonication. The amount of ethanol should be carefully selected such that the concentration of NWs will be not too high or too low. A 6% PVA (Polyvinyl alcohol) aqueous solution is then spun onto a separate Si wafer at 1000 rpm for 60s and baked on a hotplate at 75°C for three minutes. PMMA (PMMA: poly (methyl methacrylate) from Microchem, 950K A6) is then spun on the PVA surface at 1000 rpm for 60s and baked at 75°C on a hotplate for ten minutes. A droplet of ethanol solution with the Ge/Si NWs is dropped on the PMMA surface. After naturally drying, the target NW is located in the dark field under an optical microscope (Olympus BX-51). The PMMA film is then peeled from the PVA surface with an adhesive tape (Nitto BTK-180E-BLK) attached on a frame carrier while the silicon wafer with the bilayer polymer matrix is heated up to 80°C. The frame carrier is then mounted onto a three-dimensional (3D) micro-manipulator and the NWs on the suspended PMMA film are located in the microscope. Thanks to the sub-micron XY accuracy of the manipulator, the selected NW can be aligned just above the pre-defined gates of the devices and slowly brought into contact with the target chip, which is being heated up to 150°C to ensure the good contact between PMMA film and the chip surface. After the PMMA has adhered to the surface, we slowly lift the frame carrier and the NW and PMMA is left on the Si wafer. The PMMA is finally removed using acetone.

hBN flakes transfer. Hexagonal Boron Nitride (hBN) flakes are first prepared using mechanical exfoliation with an adhesive tape (Nitto BTK-180E-BLK) onto a Si substrate with a 300nm-thick thermal oxidation layer. The thickness of hBN sheets is judged from the color contrast under the optical microscope. The selected hBN flakes (10~30nm in thickness) are then transferred with a PPC/PDMS bilayer polymer stamp (PPC: polypropylene carbonate and PDMS: polydimethylsiloxane) with the same home-made 3D micro-manipulator, similar technique has been reported elsewhere.[5–7] The polymer stamps are prepared as follows: A piece of PDMS (1~2mm in thickness) is first deposited on a glass slide and treated in oxygen plasma for 1min (60W, 250mTorr). A 1μm thick film of PPC is then cast on the PDMS stamp and baked for 10 minutes at 80°C. In order to pick up hBN flakes from the preparation substrate, the PDMS stamp is brought into contact with the substrate baked at 50°C; the stamp with the hBN flake is then very slowly lifted up. To successfully release the hBN on the target chips, the stamp is heated at 90 to 110°C when in contact and peeled off very slowly with hBN flakes left on the substrate.

Lithography. In the first electron-beam lithography (EBL), two sets of dense surface gates with a 100nm pitch and the intermediate patterns are defined on a highly resistive Si wafer surface followed with the electron beam deposition of a 5/25nm Ti/Au. The large bonding pads of gates (made of 5/150nm Ti/Au) with on-chip LC low pass filters are fabricated by a following photon-lithography and metallization. The transmission line resonator is patterned in the second EBL and the design ensures the pre-defined surface gates are close to each open end of the resonator. A 100nm-thick MoRe superconducting film is then deposited with DC magnetron sputtering. The width of the resonator central pin is 10μm and the gaps between central pin and ground planes are 6μm wide, yielding the characteristic impedance of approximately 50Ω. In the same step a DC bias line connected through an on-chip spiral inductor to the middle of the signal line is made so that the high quality-factor of the resonator is maintained.[8,9] After the hBN flakes and Ge/Si NWs are placed onto the surface gates, ohmic contacts are made using 1/80nm Ti/Pd with the EBL and deposition. Contacts

connect the NW to the central pin and ground planes. A 3-second dip in a diluted buffer hydrofluoric (BHF) solution (BHF: H_2O=1: 2) is used to remove the natural oxidation on the Si shell surface prior to the electron beam deposition for contacts.
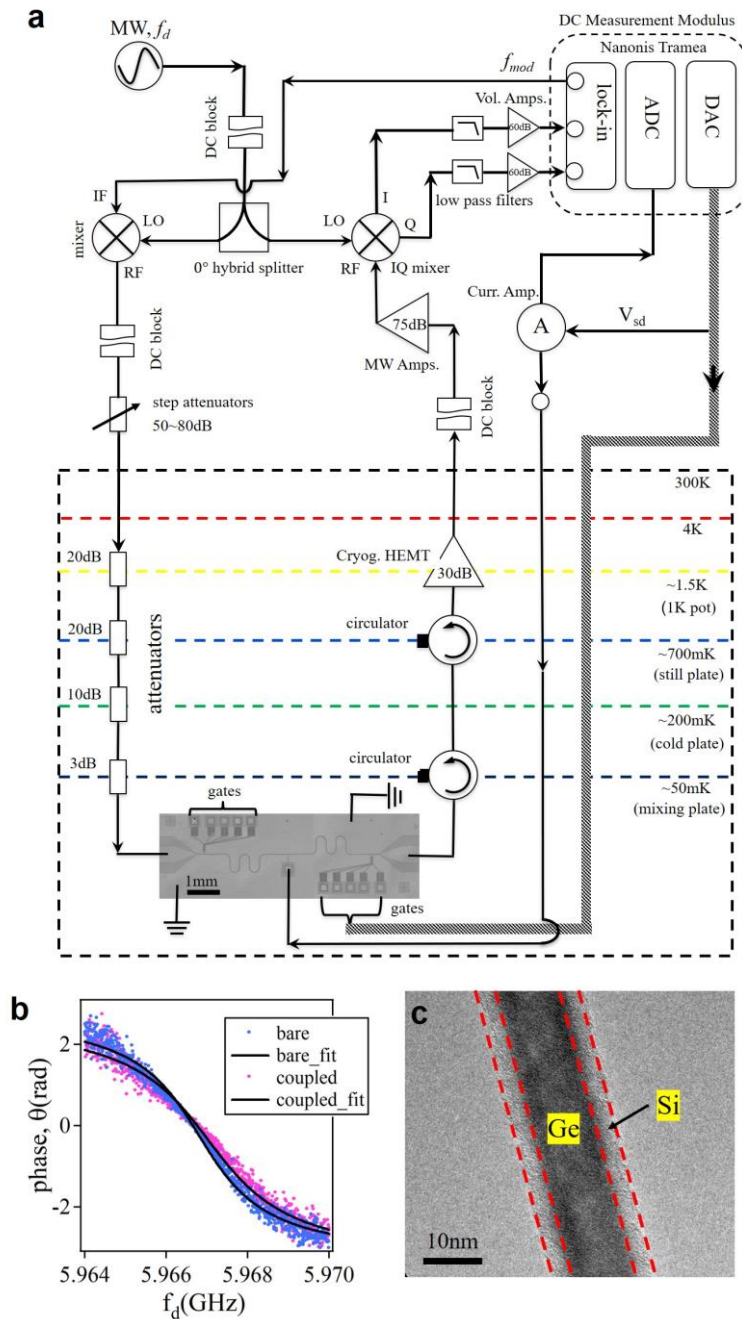
Measurement Setup

Figure S1. (a) A simplified schematic of the DC and microwave measurement setup. (b) Phase spectrum of resonance transmission as a function of f_d when ε=0 and $\varepsilon \gg 0$, corresponding to Figure 1(c). (c) TEM of one Ge/Si NW. The red dashed lines in (c) define the interface between Ge core and Si shell.

The measurement is performed on an Oxford instruments MX100 dilution refrigerator equipped with semi-rigid coaxial lines with good thermal anchors to the stages (simplified circuit diagram illustrated in Figure S1(a)). The input microwave line is attenuated with a total of 53dB distributed over all stages. This attenuation prevents the heating leakage to the

samples due to blackbody radiation transmitted from the higher temperature stages and room temperature (RT). Semi-rigid coaxial lines below the 1K stage are all superconducting NbTi cables. The output lines are buffered by two cryogenic isolators mounted at the mixing chamber and the still stage to block noise transmission from the cryogenic amplifier mounted at 1.5K. The signal transmitted through the cavity is first amplified by 30dB at the 1.5K stage using a commercial cryogenic HEMT followed with three-stage microwave amplifiers (~75dB in total) at RT. The sample is enclosed in a tightly shielded copper holder mounted on a cold finger below the mixing chamber with a base temperature of ~50mK.

The DQD was characterized by direct transport and the response of the microwave resonator, simultaneously. The DC current through the DQD down to picoamperes was measured using a biased current amplifier at RT. The resonator transmission is measured with a lock-in homodyne technique. We use a Nanonis Tramea systems (SPECS Zurich) providing the modulation and demodulation for the lock-in measurements with the internal DAC (digital-analog convertor) and ADC (analog-digital convertor) elements. The microwave drive was first modulated in amplitude with a mixer by a slow sinusoidal wave from Tramea with a frequency f_{mod}=1170Hz and an amplitude V_{mod}=0.7V (the maximal value can be applied to the mixer IF port before the nonlinear modulation) at RT. The modulated drive was then attenuated at each stage of the dilution refrigerator before reaching the input port of the device. With a variable attenuator at RT the input power P_{in} spanned a range -100~-130dBm. The transmitted signal out of the resonator was amplified by the HEMT and RT amplifiers and then demodulated by an IQ mixer to obtain the quadrature components, I and Q. The sinusoidal I and Q signals were further amplified by voltage amplifiers (60dB) and demodulated by a lock-in amplifier to extract out the amplitude, A_I and A_Q. The amplitude and the phase of the transmitted signals is determined as $A=\sqrt{A_I^2+A_Q^2}$ and $\theta=\arctan(\frac{A_Q}{A_I})$, respectively. For the frequency domain measurements, we perform slow CW (continuous wave) ramps with sweeping frequency using a microwave signal generator which is triggered by a sharp voltage step applied from a Tramea DAC output, allowing synchronization of the whole system. FigureS1(b) presents the comparison of the phase spectra as a function of microwave drive frequency f_d when the qubit is at $\varepsilon\gg0$ (blue dots) and $\varepsilon=0$ (red dots), corresponding to the same gate conditions shown in Figure 1(c) for the transmission power comparison.

DQD Out of Equilibrium
Figure S2 shows the DC current and microwave response in amplitude and phase when the DQD is biased with Vsd=0.5, 0 and -0.5mV, respectively. The microwave drive power P_{in}=-125dBm with f_d=f_c. Figure S2(a-c) display the current diagrams with voltage sweeping ranges of plunger gates similar to Figure 1(d) and the other gate voltages V_{SB}=4.3V, V_B=7.145V, V_{DB}=3.5V, respectively. The colorscale represents a variation of current in a range of ±20 pA. The lever arms of the plunger gates can be derived from the size of the transport triangles as indicated in the current plots:[10]

$$\alpha_{L(R)}=\frac{eV_{sd}}{\delta V_{L(R)}}=0.079(0.077)eV/V. \tag{S1}$$

The capacitance of each plunger gate is determined by the charge transition spacing:

$$C_{L(R)}=\frac{e}{\Delta V_{L(R)}}=4.7(4.6)aF. \tag{S2}$$

The total capacitance from gate, source and drain of each quantum dot is:

$$C_{L(R)}^{\Sigma}=\frac{C_{L(R)}}{\alpha_{L(R)}}=59.5(59.7)aF. \tag{S3}$$

The mutual electrostatic coupling capacitance between the adjacent dots is determined by the length of the interdot line:

$$C_m = C_R^\Sigma \frac{\Delta V_L^m}{\Delta V_L} = C_L^\Sigma \frac{\Delta V_R^m}{\Delta V_R} \approx 20aF. \tag{S4}$$

The cross capacitive coupling rate is defined as:

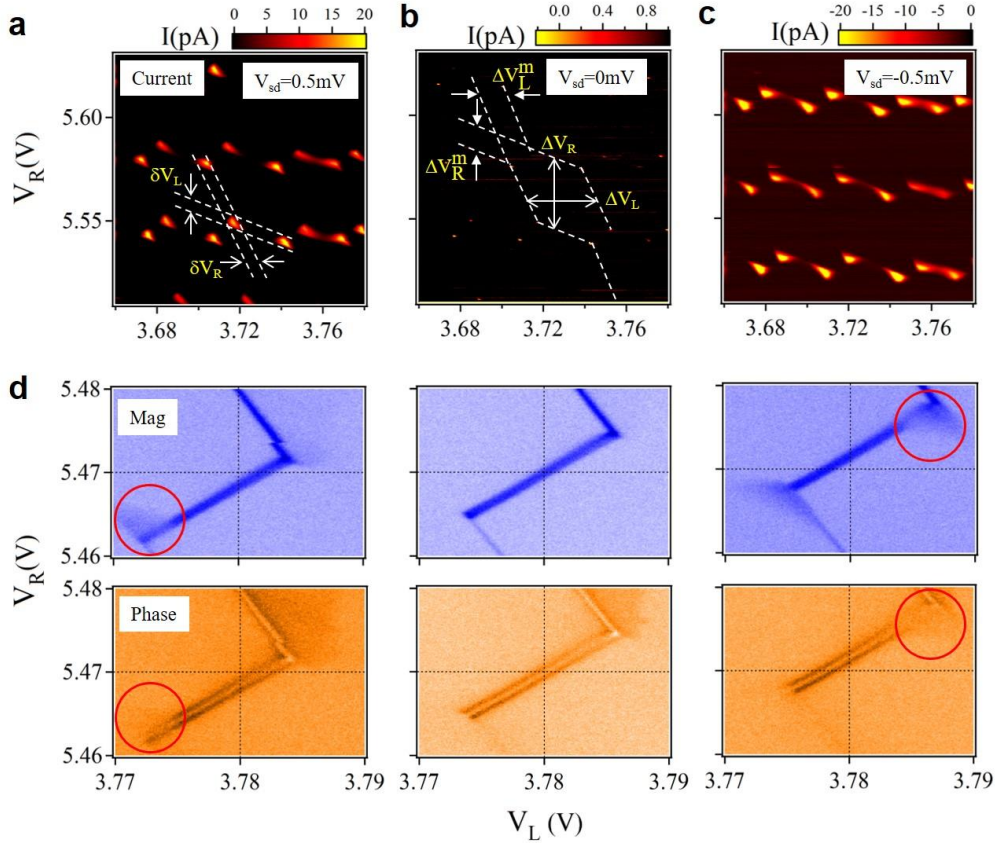$$\beta_m = \frac{C_m}{C_{L(R)}^\Sigma} \approx 0.333. \tag{S5}$$

Figure S2. DC current plots as a function of V_L and V_R representing the charge stability diagram with (a) V_{sd} =-0.5mV, (b) V_{sd} =0mV and (c) V_{sd} =0.5mV. The charging energies of QDs and the lever-arms are extracted from the hexagonal patterns. (d) Magnitude and phase variations of one inter-dot charge transition line under different biases corresponding to (a-c). The circles in (d) highlight the transport triangles observed from the cavity response, showing a similar triangle patterns as observed in the DC transport spectroscopy.

The charging energy of each dot is:

$$E_{L(R)} = e^2 \frac{C_{R(L)}^\Sigma}{C_L^\Sigma C_R^\Sigma - C_m^2} = 2.6(2.8)meV. \tag{S6}$$

The mutual electrostatic energy is:

$$E_m = e^2 \frac{C_m}{C_L^\Sigma C_R^\Sigma - C_m^2} \approx 0.9meV. \tag{S7}$$

Upon applying the source-drain bias, the positions of the interdot transition lines in the charge diagram also shift due to the capacitive gating from the contact electrodes. Figure 2d shows the respective magnitude and phase evolution of one interdot line under different V_{sd}. The

shift of the position according to the plunger gate voltages (denoted as V_L' and V_R') represents the change of the QD chemical potentials. The energy detuning between the left-right QD induced by V_{sd} is regulated by a lever-arm as:

$$\alpha_S = \frac{\Delta\mu_L - \Delta\mu_R}{V_{sd}} = \frac{\alpha_L V_L' - \alpha_R V_R'}{V_{sd}} = 0.243\,eV/V \tag{S8}$$

It is worthwhile to note that we observe a significant signal reduction in both magnitude and phase spectroscopies close to the regions (indicated by circles in Figure S2(d)) where the charge transport triangles always occur under finite bias as shown in Figure S2(a) and (c). The same cavity response to the DC transport has also been observed on a carbon nanotube DQD.[11] The observations can be interpreted that with a finite bias V_{sd} and detuning ε, the ground and excited states of qubit will be out-of-equilibrium as the charge will sequentially hop through the down-hill energy scape of the DQD between the electrodes. The qubit occupation probability $\langle\sigma_z\rangle$ is determined by the qubit energy relaxation rate and tunneling rates between the QDs and the electrodes. In the triangle regions, the qubit will remain in the excited state for certain period and $\langle\sigma_z\rangle$ is not close to -1. According to Eq. (3) in the main text, the resonance dispersive shift induced by the qubit will be altered, resulting in magnitude and phase variations. Outside the transport triangles where the DQD is isolated from the electrodes and the charge transport is forbidden, the signals remain similar to those in the spectroscopy when $V_{sd}=0$.

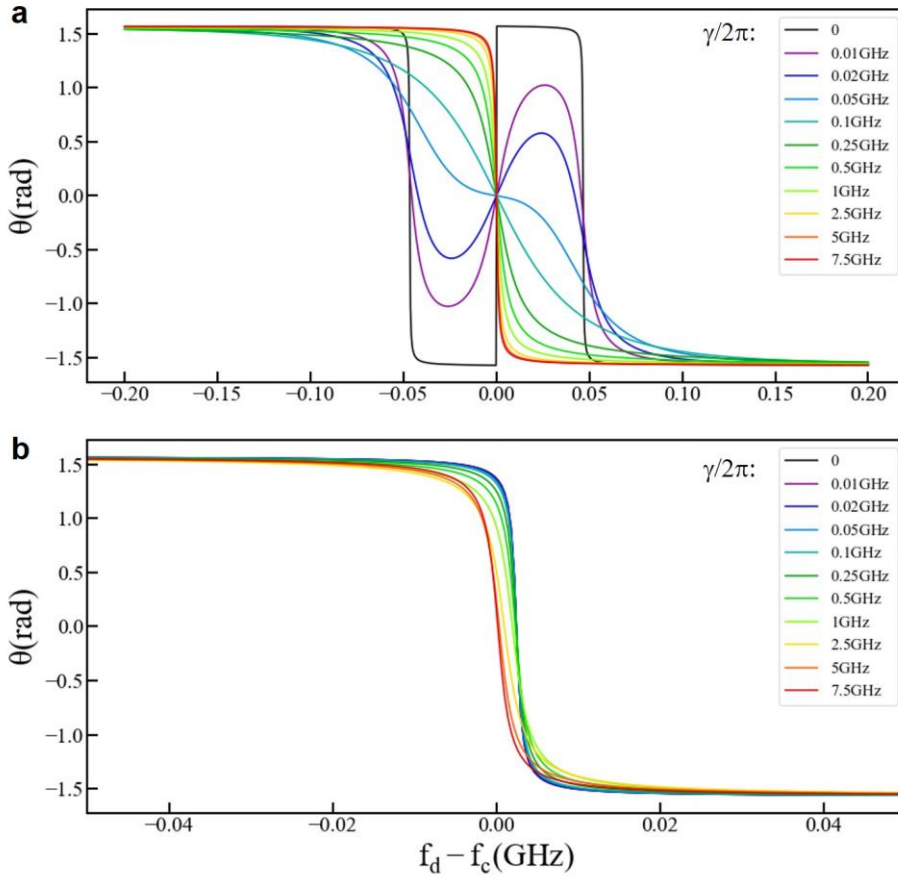**Resonator Phase Spectrum with Different Qubit Decoherence**

Figure S3. Numerical calculation of full phase spectra with different γ in the case of (a) on resonance $\Delta=0$ and (b) detuned $\Delta\neq0$ regime, corresponding to the transmission power spectra in Figure 3(d) and (e).

In Figure 3 (d) and (e) we present the calculated transmission power as a function of f_d in the case of (a) on resonance, $\Delta=0$ and (b) detuned, $\Delta\neq0$ with different qubit decoherence rate, γ. Figure S3 shows the corresponding phase spectra. In the former case when $\gamma<2g_{eff}$, we observe that the phase experiences two cycles of variation from the maxima to the minima when sweeping f_d, which is in accordance with the Rabi splitting observed in the power spectra as shown in the main text. Once γ becomes larger than $2g_{eff}$ and the splitting peaks merge into one, the phase spectra only show a single $\pi/2$ to $-\pi/2$ transition. The gradient of the tendency reflects the qubit decoherent rate. In the case of $\Delta\neq0$, the cavity mode experiences only a dispersive shift. We then only see a single phase-transition with slight variations in the trends as seen in Figure S3(b).

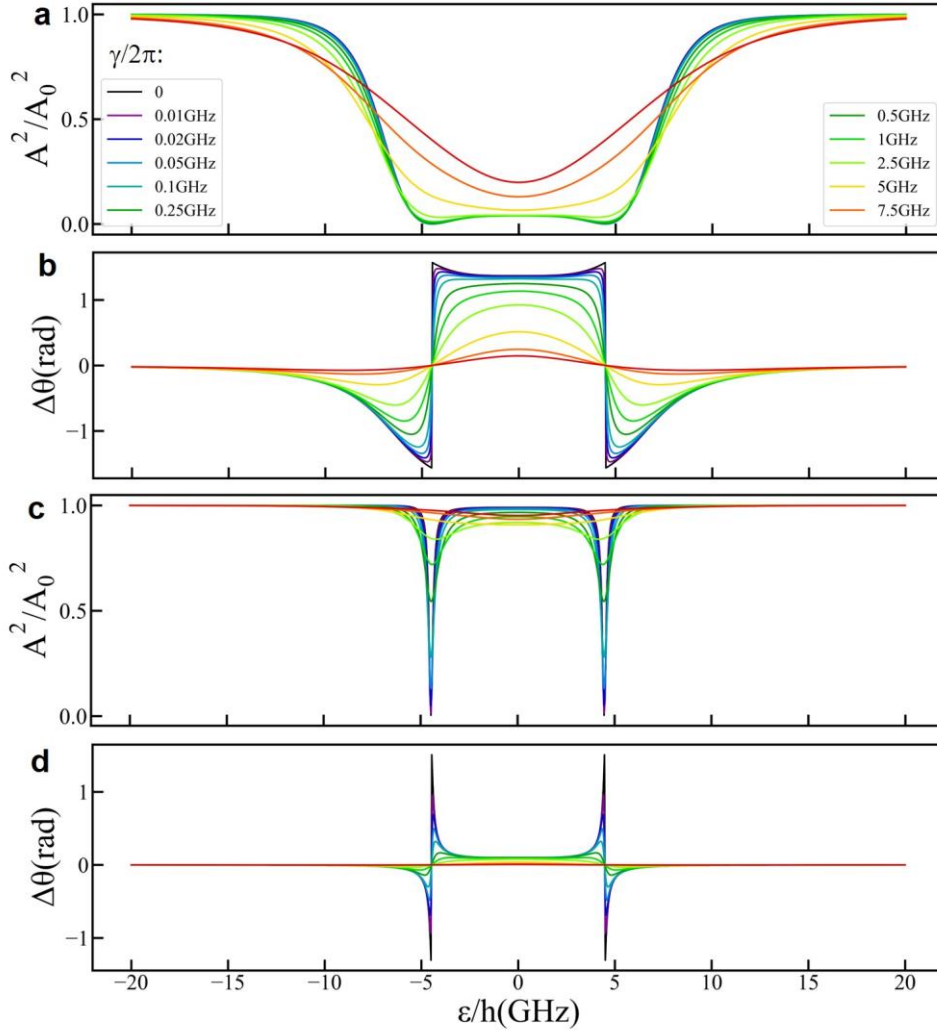**Resonator Signal Response with Different Coupling Strength**

Figure S4. Numerical calculations of (a) relative transmission power A^2/A_0^2 and (b) phase variation $\Delta\theta$ as a function of ε and γ with $g_c/2\pi=50$MHz. (c) A^2/A_0^2 and (d) $\Delta\theta$ with $g_c/2\pi=10$MHz. Other physical parameters for simulation are $[2t_c/\hbar, \omega_c, \omega_d, \kappa] =2\pi\times[4, 6, 6, 0.001]$GHz. With $g_c/2\pi=50$MHz and $\gamma/2\pi=5$GHz, the simulation well agrees with the observed results of Figure2, justifying the validity of the fits using Eq. (4).

To verify the fits of the experimental results in Figure 2, we investigate the numerically calculated cavity transmission in power and phase as a function of qubit detuning ε with different γ and g_c. The physical parameters for simulation are $[2t_c/\hbar, \omega_c, \omega_d, \kappa] =2\pi\times[4, 6, 6, 0.001]$GHz, close to the qubit state indicated by the red arrow of Figure (2). We compared the

difference of the transmitted signal with $g_c/2\pi$=50MHz for (a) and (b) and with $g_c/2\pi$=10MHz for (c) and (d) in Figure S4. With a small g_c we can observe sharp splitting features in both (c) relative power transmission A^2/A_0^2 and (d) phase variations $\Delta\theta$ plots as the qubit energy is swept across the photon level. In contrast, with a large g_c we only observe spitting in the phase curve but a single dip in the transmission power plot, which is in line with the experimental observations in Figure 2. For both cases we observe that the signal dramatically reduces as the qubit decoherence γ increases, according to the theory from Eq. (4). However, it is clearly to see that with $g_c/2\pi$=10MHz both A^2/A_0^2 and $\Delta\theta$ become very small, in contrast to the experiment results with $\gamma/2\pi$=4~7GHz. With $g_c/2\pi$=50MHz, the numerical calculations capture the main features from the measurement.

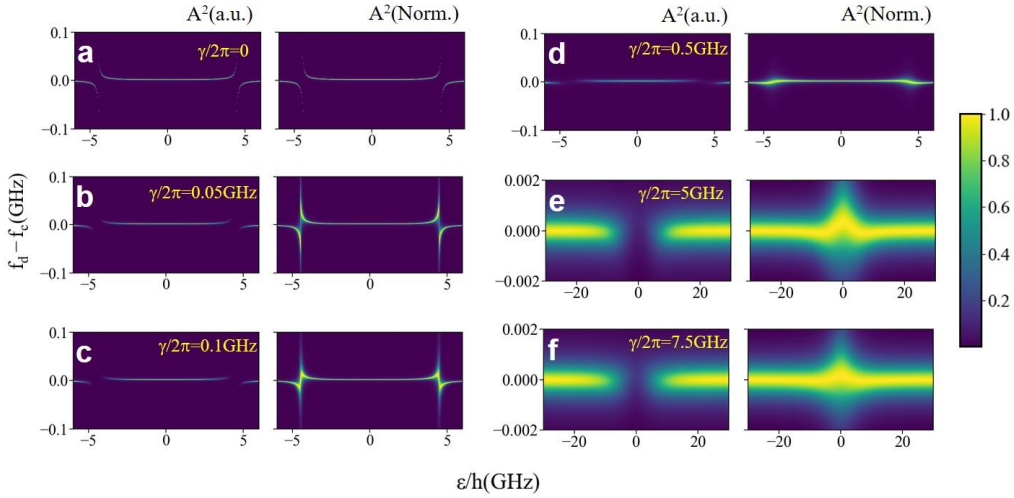**Evolution of Resonance Full Spectrum with Different Decoherence**

Figure S5. Numerically calculated full spectra as a function of f_d and ε. The evolutions of the resonance spectra with different γ are shown from (a) to (f). In each subplot, the left panel is the absolute transmission power in arbitrary units while the right one is the normalized power.

To further understand the impact of the qubit decoherence on the dynamics of the resonator transmission, we calculate the full spectrum of the resonance as a function of f_d for a set of qubit detuning ε with different decoherence rate γ. The simulation parameters are $[2t_c/\hbar, g_c, \omega_c, \omega_d, \kappa]$=$2\pi\times$[4, 0.05, 6, 6, 0.001]GHz, which are close to the qubit state and experimental conditions in Figure 4. In Figure S5, the left panel in each sub-plot shows the absolute transmission power in arbitrary units, which provides information on the dissipation. The right panels are the corresponding normalized transmission spectrum (the spectrum at each ε is normalized to its maximal transmission power), which highlights the changes in resonance lineshape. From (a) to (f) the qubit decoherence rate increases from γ=0 to $\gamma\gg g_c$. With γ=0, a clear Rabi splitting with an anti-crossing gap of $2g_{eff}$ is observed in both panels of (a). The effect as decoherence increases to be comparable to $2g_{eff}$ is shown in (b-d). In the absolute power plots the splitting features are still seen arising from the large dissipation when photons are close to resonance with the qubit. However, in the normalized plots the peaks obviously broaden and finally merge into one. When the qubit decoherence becomes much faster than the coherent interaction rate, the effect of the qubit on the cavity mode becomes much weaker. As shown in (e) and (f), the splitting features completely disappear with a pronounced reduction of transmission power and a few hundred KHz resonance frequency shift observed when ε is close to zero. The similarity between the calculation in (f) and the experimental observations further prove the validity of the fits in Figure 2.

Power Dependence of the Dispersive Shift

In Figure 5(a) and (b) of the main text we have presented the numerical calculation of $\langle\sigma_z\rangle$ and $\Delta\theta$ as a function of photon number n with different γ_1 but a fixed γ, where for all γ_1 the initial phase shifts are the same and the $\langle\sigma_z\rangle$ and $\Delta\theta$ transition tendency is only related to γ_1. Figure S6 (a-c) show a complimentary calculation of $\langle\sigma_z\rangle$ and $\Delta\theta$ as a function of n with different γ but a fixed γ_1. In contrast to the former case, we observe that the initial phase shifts for each γ are different, in good agreement with the prediction of Eq. (4). With the same γ_1 the positions for the $\langle\sigma_z\rangle$ and $\Delta\theta$ transition relative to photon number n axis is almost the same. This discrepancy indicates that the power dependence of the resonance dispersive shift is a powerful probe to sperate γ_1 and γ_Φ as $\gamma_\Phi = \gamma - \gamma_1/2$. For large n we utilize an analytical simulation using the combination of Eq. (4) and (5) (here photon number n is an input parameter). Figure S6(d) and (e) present the analytical calculated $\langle\sigma_z\rangle$ and $\Delta\theta$ as a function of n, which reveals the same relations as shown in Figure 5 of the main text. The dependence of $\Delta\theta$ on $\langle\sigma_z\rangle$ for different γ_1 with analytical and numerical calculations is compared in Figure S6(f). It is clearly seen that although the ranges of $\Delta\theta$ and $\langle\sigma_z\rangle$ are different because of various qubit energy relaxations, the dependence strictly follows Eq. (4) and (5).
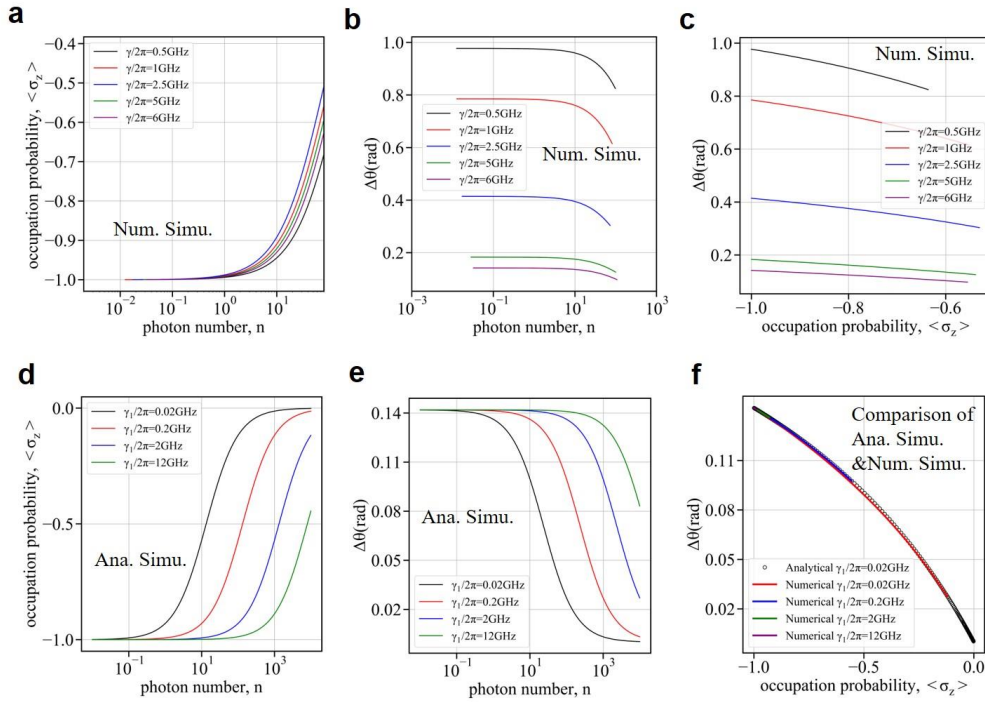

Figure S6. Numerically calculated (a) qubit occupation probability $\langle\sigma_z\rangle$ and (b) phase shift $\Delta\theta$ as a function of n with different γ and a fixed $\gamma_1=2\pi\times0.02$GHz. (c) $\Delta\theta$ vs. $\langle\sigma_z\rangle$ with different γ, showing different initial phase. The other simulation parameters are the same as those in Figure 5 in the main text. Analytical calculations using Eq. (4) and (5) are present in (d) $\langle\sigma_z\rangle$ and (e) $\Delta\theta$ as a function of photon number n with a fixed γ but different γ_1, where $\gamma=\gamma_1/2+\gamma_\Phi$. (d) and (e) show the consistent results as those in Figure 5 (a) and (b). (f) Comparison of $\Delta\theta$-$\langle\sigma_z\rangle$ dependence using the numerical and analytical calculation results. They show exactly same tendency.

References

(1)   Lauhon, L. J.; Gudiksen, M. S.; Wang, D.; Lieber, C. M. Epitaxial Core–Shell and Core–Multishell Nanowire Heterostructures. *Nature* **2002**, *420* (6911), 57–61.

(2)   Taychatanapat, T.; Watanabe, K.; Taniguchi, T.; Jarillo-Herrero, P. Quantum Hall Effect and Landau-Level Crossing of Dirac Fermions in Trilayer Graphene. *Nat. Phys.* **2011**, *7* (8), 621–625.

(3)   Wang, R.; Deacon, R. S.; Car, D.; Bakkers, E. P. a. M.; Ishibashi, K. InSb Nanowire Double Quantum Dots Coupled to a Superconducting Microwave Cavity. *Appl. Phys. Lett.* **2016**, *108* (20), 203502.

(4)   Wang, R.; Deacon, R. S.; Yao, J.; Lieber, C. M.; Ishibashi, K. Electrical Modulation of Weak-Antilocalization and Spin–Orbit Interaction in Dual Gated Ge/Si Core/Shell Nanowires. *Semicond. Sci. Technol.* **2017**, *32* (9), 094002.

(5)   Pizzocchero, F.; Gammelgaard, L.; Jessen, B. S.; Caridad, J. M.; Wang, L.; Hone, J.; Bøggild, P.; Booth, T. J. The Hot Pick-up Technique for Batch Assembly of van Der Waals Heterostructures. *Nat. Commun.* **2016**, *7*, 11894.

(6)   Kim, K.; Yankowitz, M.; Fallahazad, B.; Kang, S.; Movva, H. C. P.; Huang, S.; Larentis, S.; Corbet, C. M.; Taniguchi, T.; Watanabe, K.; Banerjee, S. K.; LeRoy, B. J.; Tutuc, E. Van Der Waals Heterostructures with High Accuracy Rotational Alignment. *Nano Lett.* **2016**, *16* (3), 1989–1995.

(7)   Amet, F.; Ke, C. T.; Borzenets, I. V.; Wang, J.; Watanabe, K.; Taniguchi, T.; Deacon, R. S.; Yamamoto, M.; Bomze, Y.; Tarucha, S.; Finkelstein, G. Supercurrent in the Quantum Hall Regime. *Science* **2016**, *352* (6288), 966–969.

(8)   Mi, X.; Cady, J. V.; Zajac, D. M.; Stehlik, J.; Edge, L. F.; Petta, J. R. Circuit Quantum Electrodynamics Architecture for Gate-Defined Quantum Dots in Silicon. *Appl. Phys. Lett.* **2017**, *110* (4), 043502.

(9)   Chen, F.; Sirois, A. J.; Simmonds, R. W.; Rimberg, A. J. Introduction of a Dc Bias into a High-Q Superconducting Microwave Cavity. *Appl. Phys. Lett.* **2011**, *98* (13), 132509.

(10)   van der Wiel, W. G.; De Franceschi, S.; Elzerman, J. M.; Fujisawa, T.; Tarucha, S.; Kouwenhoven, L. P. Electron Transport through Double Quantum Dots. *Rev. Mod. Phys.* **2002**, *75* (1), 1–22.

(11)   Viennot, J. J.; Delbecq, M. R.; Dartiailh, M. C.; Cottet, A.; Kontos, T. Out-of-Equilibrium Charge Dynamics in a Hybrid Circuit Quantum Electrodynamics Architecture. *Phys. Rev. B* **2014**, *89* (16), 165404.